

Optical properties of two-dimensional Dirac-Weyl materials with a flat band

Li-Li Ye,¹ Chen-Di Han,¹ and Ying-Cheng Lai^{1,2, a)}

¹⁾*School of Electrical, Computer and Energy Engineering, Arizona State University, Tempe, AZ 85287, USA*

²⁾*Department of Physics, Arizona State University, Tempe, Arizona 85287, USA*

(Dated: 23 February 2024)

The emergence of a flat band in Dirac-Weyl materials offers new possibilities for electronic transitions, leading to stronger interaction with light. As a result, the optical conductivity can be significantly enhanced in these flat-band materials as compared with graphene, making them potentially better candidates for optical sensing and modulation. Recently, a comprehensive theory for the optical conductivity of a spectrum of flat-band Dirac-Weyl materials has been developed, with explicit formulas for both the real and imaginary parts of the conductivity derived through two independent approaches. This Perspective offers a review of the development. An understanding of the optical properties of the flat-band Dirac-Weyl materials paves the way for optical device applications in the terahertz-frequency domain.

I. INTRODUCTION

A frontier area of research in applied physics is two-dimensional (2D) Dirac-Weyl materials whose energy band consists of a pair of Dirac cones and a topologically flat band, electronic or optical^{1–28}. A flat band can also arise in metal-organic and covalent-organic materials^{29,30}. This Perspective focuses on the optical properties but with a brief review of a number of phenomena related to the electronic and magnetic properties of these materials.

To develop optical sensors and modulators based on Dirac-Weyl materials, the problem of adequate optical absorption must be addressed. Graphene, due to its linear dispersion relationship, has potential applications in developing optical devices^{31–33}. For example, graphene-based polarizers have the ability to select light polarization in a broad frequency range³⁴. Graphene can also support high-frequency plasmon modes with frequency ranging from several terahertz to infrared, making it appealing for high-frequency communications^{35,36} and ultrafast transform optics^{37,38}. The ability to generate strong polarization of light implies that materials coated with graphene can be exploited for applications at the two extremes: cloaking or superscattering^{39–41}. A difficulty in such applications is that the light absorption rate of a single-layer graphene is quite low - only a few percent. To significantly enhance the optical absorption has attracted a great deal of interest since the beginning of the field of 2D Dirac-Weyl materials. For example, it was found that^{42,43}, when graphene is coupled with a proper dielectric material, surface plasmon mode can arise so that the achievable optical absorption rate can be over 90%. Such surface plasmon can also propagate in a graphene lattice with frequency above the terahertz domain^{44–46}, implying potential applications in high frequency communication devices. It was also found that,

in slightly twisted bilayer graphene, unusual plasmon modes and strong optical absorption can arise^{47–49}.

In the study of the optical properties of graphene, the conventional way was to treat the material as a thin layer with electric conductivity depending on the angular frequency ω of the incident field, leading to the optical conductivity $\sigma(\omega)$ that is typically complex⁵⁰. When the energy of the incident photon is below the Fermi energy μ : $\hbar\omega < \mu$, only the intraband electron transition (from the conduction band to itself) is allowed. Such a process usually occurs for large devices in the frequency range of subterahertz and terahertz (0.1-10 THz)^{43,51}. For incident wave with a higher frequency, e.g., $\hbar\omega \approx 2\mu$, intraband transitions become insignificant and interband transitions from the valence to the conduction band dominate. For smaller devices, the optical field can be in the infrared to visible range^{52,53}. Graphene plasmons are tunable by changing the Fermi energy, but the plasmon density is frequency-dependent due to the different carrier densities at different frequencies. A 1D topological electric with density-independent frequency was reported⁵⁴. The simulation result was further verified by first-principle calculations on Ba_3CrN_3 and Sr_3CrN_3 . Density-independent plasmons were predicted to arise in both 2D nodal line and 1D nodal point systems and confirmed by first-principle calculations⁵⁵. In general, to fully characterize the electromagnetic properties of the material, both the real and imaginary parts of the optical conductivity are required.

In a recent work⁵⁶, a comprehensive theory for the optical conductivity of a spectrum of 2D Dirac-Weyl materials was developed. It is the so-called $\alpha\text{-}\mathcal{T}_3$ lattice system with graphene sitting at one end and pseudospin-1 material at the other end of the spectrum². An $\alpha\text{-}\mathcal{T}_3$ lattice is formed from the honeycomb graphene lattice by adding an extra atom at the center of each hexagonal unit cell², with the normalized coupling strength αt between this atom and any nearest neighboring atom in the cell, where $0 \leq \alpha \leq 1$ and t is the nearest-neighbor hopping energy in the original graphene lattice. The low energy excitations of the $\alpha\text{-}\mathcal{T}_3$ lattice can be described by the generalized Dirac-Weyl equation^{2,57}, where the

^{a)}Electronic mail: Ying-Cheng.Lai@asu.edu

spinor wave function has three components. The lattice degenerates to graphene with pseudospin-1/2 quasiparticles for $\alpha = 0$ - only in this limiting case is a flat band absent. For $\alpha > 0$, a flat band through the conic interaction of the two Dirac cones exists^{10,58}. Under a continuum approximation, an $\alpha\mathcal{T}_3$ lattice is effectively a thin conducting layer. Because of the flat band, three types of band-to-band transitions can occur: intraband, cone-to-cone, and flat-band-to-cone transitions. A general finding was that the extra transitions brought upon by the flat band can enhance the optical conductivity⁵⁶.

Experimentally, photonic crystals can be used to generate $\alpha\mathcal{T}_3$ lattices^{27,59-61}. Electronically, candidate materials include transition-metal oxide SrTiO₃/SrIrO₃/SrTiO₃ trilayer heterostructures⁶, SrCu₂(BO₃)₂¹² or graphene-In₂Te₂¹³. Realization of other flat-band lattice systems is also possible^{62,63}.

This Perspective is organized, as follows. In Sec. II, several experimental lattice systems of 2D Dirac-Weyl flat-band materials are introduced. The full optical-conductivity theory of these materials is reviewed in Sec. III. Opinion on potential future research is offered in Sec. IV.

II. EXPERIMENTALLY ACCESSIBLE LATTICE SYSTEMS OF 2D DIRAC-WEYL FLAT-BAND MATERIALS

Figure 1 shows three commonly studied lattice structures of 2D Dirac-Weyl flat-band materials - dice, Lieb, and Kagome lattices, together with their corresponding energy-band structures. The details of these lattices are described below.

A. Dice lattice

Dice lattice was originally proposed to study the Green's function for diatomic lattice systems⁶⁴. The lattice is constructed by removing some couplings from a triangular lattice. The emergence of a flat band and a localization phenomenon in the dice lattice were first report in Ref. [1]. The localization behavior was later found to persist in the dice lattice system in the presence of a magnetic field⁶⁵. A similar phenomenon was also reported in quantum networks⁶⁶, in systems with spin-orbit coupling⁶⁷, and in a Bose-Hubbard model⁵⁹. About 14 years ago, interest in the dice lattice was rejuvenated due to its unique structure of a pair of Dirac cones and a flat band².

Dice lattice has three nonequivalent atoms, as shown in Fig. 2(a). The lattice has a three fold rotational symmetry and is also called the \mathcal{T}_3 lattice. The tight binding Hamiltonian describing the electronic structure of the dice lattice, taking into account nearest-neighbor hop-

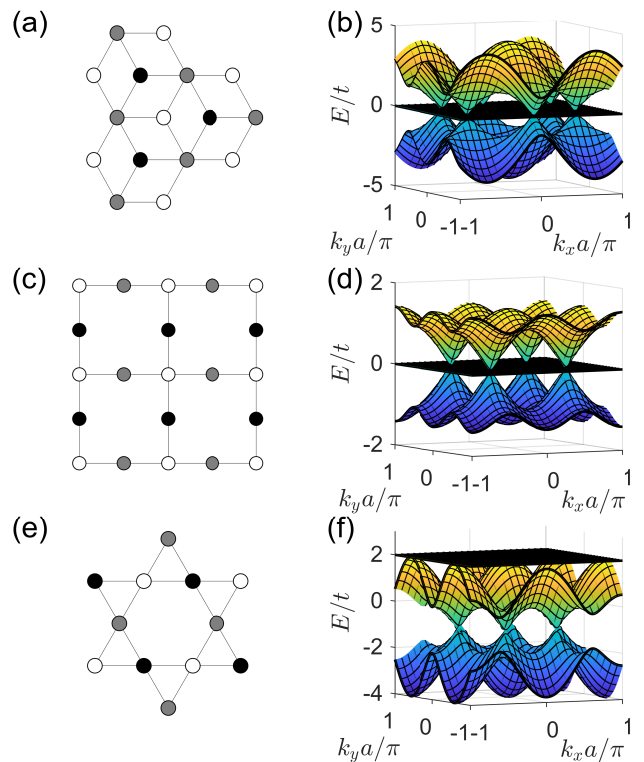


FIG. 1. Schematic illustration of three different lattice structures of 2D Dirac-Weyl materials with a flat band. (a,b) Dice lattice and its band structure, respectively. The first Brillouin zone has a honeycomb structure and two distinct valleys. (c,d) Lieb lattice and its band structure, respectively. The first Brillouin zone is a square with only one valley. (e,f) Kagome lattice and its band structure, respectively. The first Brillouin zone is a honeycomb with the same orientation as the original lattice, but the flat band arises at the top of the conduction band.

ping, is given by

$$\mathcal{H}(\mathbf{k}) = -t(e^{i\mathbf{k}\cdot\boldsymbol{\delta}}a_{\mathbf{k}}^{\dagger}b_{\mathbf{k}} + e^{-i\mathbf{k}\cdot\boldsymbol{\delta}}b_{\mathbf{k}}^{\dagger}a_{\mathbf{k}} + e^{i\mathbf{k}\cdot\boldsymbol{\delta}}b_{\mathbf{k}}^{\dagger}c_{\mathbf{k}} + e^{-i\mathbf{k}\cdot\boldsymbol{\delta}}c_{\mathbf{k}}^{\dagger}b_{\mathbf{k}}) \quad (1)$$

where t is the nearest-neighbor hopping energy, $a^{\dagger}, b^{\dagger}, c^{\dagger}$ and a, b, c are creating and annihilation operators, respectively, and $\boldsymbol{\delta}$ is a vector in the physical space with $|\boldsymbol{\delta}| = a$. Expanding $\boldsymbol{\delta}$ in the basis $(a_{\mathbf{k}}, b_{\mathbf{k}}, c_{\mathbf{k}})$ leads to the Hamiltonian:

$$H_{\text{Dice}} = -t \begin{pmatrix} 0 & \Delta_{\mathbf{k}} & 0 \\ \Delta_{\mathbf{k}}^* & 0 & \Delta_{\mathbf{k}} \\ 0 & \Delta_{\mathbf{k}}^* & 0 \end{pmatrix} \quad (2)$$

where $\Delta_{\mathbf{k}} = 2 \exp(-ik_x a/2) \cos(\sqrt{3}/2 k_y a) + \exp(ik_x a)$. The energy eigenvalues are $E_{\pm} = \pm t \sqrt{\Delta_{\mathbf{k}} \Delta_{\mathbf{k}}^*}$ and $E_0 = 0$. Figure 2(b) shows the first Brillouin zone. At each of the six corners, the conduction and valence bands touch

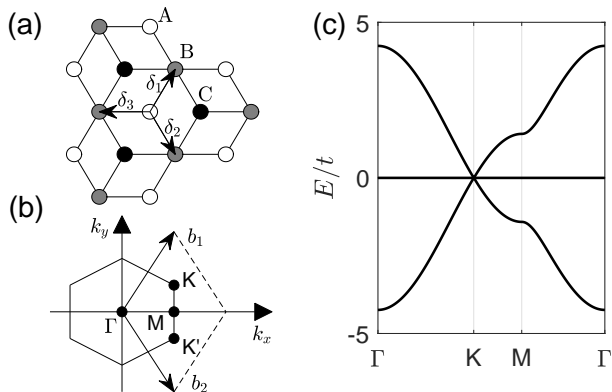


FIG. 2. A more detailed view of dice lattice and its band structure. (a) Dice lattice and the three nonequivalent atoms. The lattice unit vectors are δ_i ($i = 1, 2, 3$). (b) The first Brillouin zone. There are two nonequivalent Dirac points: \mathbf{K} and \mathbf{K}' . (c) The band structure, where the conduction and valence bands as well as a flat band touch each other at a Dirac point.

each other at the Dirac points \mathbf{K} and \mathbf{K}' (corresponding to two distinct valleys), which are given by

$$\mathbf{K} = \left(\frac{2\pi}{3a}, \frac{2\pi}{3\sqrt{3}a} \right), \mathbf{K}' = \left(\frac{2\pi}{3a}, -\frac{2\pi}{3\sqrt{3}a} \right), \quad (3)$$

and there is a flat band through the Dirac point, as shown in Fig. 2(c). For low energy excitations, the momentum relative to a Dirac point is $\mathbf{q} = \mathbf{k} - \mathbf{K}$, so one can write $\Delta_{\mathbf{k}} \equiv \Delta_{\mathbf{q}}$. Expanding $\Delta_{\mathbf{q}}$ about \mathbf{K} gives $\Delta_{\mathbf{q}} \approx q_x - iq_y$ so the energy becomes $E_{\pm} \approx \pm v_F |q|$. The effective Hamiltonian for low energy excitations can then be written as

$$H = v_F \mathbf{S} \cdot \mathbf{q}, \quad (4)$$

where

$$S_x = \frac{1}{\sqrt{2}} \begin{pmatrix} 0 & 1 & 0 \\ 1 & 0 & 1 \\ 0 & 1 & 0 \end{pmatrix}, S_y = \frac{1}{\sqrt{2}} \begin{pmatrix} 0 & -i & 0 \\ i & 0 & -i \\ 0 & i & 0 \end{pmatrix},$$

\mathbf{S} follows general type of Levi-Civita symbols, and v_F is the Fermi velocity. A similar energy expansion can be carried for the other valley \mathbf{K}' , leading to $H_{\mathbf{K}'} = v_F(S_x q_x - S_y q_y)$. For the dice lattice, there exist two distinct valleys - each triply degenerated.

B. Lieb lattice

The Lieb lattice originated the Lieb theorems of ferromagnetism for certain lattice structures⁶⁸. The first explicit lattice structure was studied in Ref. [69]. Subsequently, a photonic crystal realization of the Lieb lattice was proposed^{3,70}. The unit cell of the Lieb lattice has

three nonequivalent atoms forming a square-like structure, as shown in Fig. 1(c). The tight binding Hamiltonian is

$$\mathcal{H}_{\text{Lieb}} = -2t \begin{pmatrix} 0 & \cos(k_x a/2) & \cos(k_y a/2) \\ \cos(k_x a/2) & 0 & 0 \\ \cos(k_y a/2) & 0 & 0 \end{pmatrix}. \quad (5)$$

The eigenvalues are $E = \pm t \sqrt{\cos^2(k_x a/2) + \cos^2(k_y a/2)}$ and $E = 0$. In the momentum space, the conduction and valence bands touch each other at $k_x, k_y = \pm\pi/a$, corresponding to four Dirac points, as shown in Fig. 1(d). The effective Hamiltonian for the Lieb lattice⁷¹ has the same form as that for the dice lattice given by Eq. (4) through a unitary transform⁷². The difference is that, for a dice lattice there are two distinct valleys but there is only one valley for the Lieb lattice.

The Lieb lattice is experimentally accessible⁶² through fabrication techniques such as laser writing of optical waveguides^{15-17,19}. The electronic structure through the use of CO and Cu(1,1,1) molecules was studied²⁷. A first-principle calculation revealed that the synthesized 2D sp^2 carbon-conjugated covalent-organic framework (sp^2c -COF) can have the band structure similar to that of the Lieb lattice⁷³.

C. Kagome lattice

The Kagome lattice originated from the study of anti-ferromagnet in decorated honeycomb lattice⁷⁴. The lattice structure has the same woven Kagome pattern⁷⁵, as shown in Fig. 1(e). The Kagome lattice represents a prototypical system for topological insulators⁷⁶⁻⁷⁸. The unit cell has three nonequivalent atoms. The tight-binding Hamiltonian is

$$\mathcal{H}_{\text{Kagome}} = -2t \begin{pmatrix} 0 & \cos k_1 & \cos k_2 \\ \cos k_1 & 0 & \cos k_3 \\ \cos k_2 & \cos k_3 & 0 \end{pmatrix} \quad (6)$$

where $k_i = \mathbf{k} \cdot \boldsymbol{\delta}_i$, $\delta_1 = \hat{x}a$, $\delta_2 = (\hat{x} + \sqrt{3}\hat{y})a/2$ and $\delta_3 = \delta_2 - \delta_1$. The energy bands are given by $E(\mathbf{k}) = t[-1 \pm \sqrt{4\Delta_{\mathbf{k}} - 3}], 2t$ with $\Delta_{\mathbf{k}} = \cos^2 k_1 + \cos^2 k_2 + \cos^2 k_3$, where the first two bands touch each other at six Dirac points at $E = -t$ and the third band is at $E = 2t$ and is flat. The flat band thus appears at the top of the conduction band, as shown in Fig. 1(f). This feature is distinct from the dice and Lieb lattices where the flat band is located at the Dirac points.

A possible realization of the Kagome lattice through $\text{Ni}_3\text{C}_{12}\text{S}_{12}$ was proposed earlier⁷⁹, where a first-principle calculation was carried out, demonstrating that nontrivial topological states exist in both Dirac and flat bands. In a recent work⁸⁰, an experimental flat-band system

through a self-assembled monolayer of 2D hydrogen-bond organic frameworks of 1,3,5-tris(4-hydroxyphenyl) benzene (THPB) on Au(111) surface was reported. The measured band structure fits well with that of the breathing-Kagome lattice. In addition, flat-to-flat band transitions in a diatomic Kagome lattice were reported⁸¹, where the interband optical absorption coefficient exhibits a sharp peak at the gap energy, indicating a transition between the two flat bands. The results were further confirmed by first principle calculations for the material $\text{Li}_{12}\text{-(Ni}_3\text{C}_{12}\text{S}_{12})_2$. Other phenomena in the Kagome lattice include the excited quantum anomalous Hall effect⁸², an excitonic insulator⁸³, and theoretically proposed excitonic Bose-Einstein condensation⁸⁴.

D. $\alpha\text{-}\mathcal{T}_3$ lattice

In addition to the dice, Lieb, and Kagome lattices, another lattice structure that can generate a flat band through the Dirac points is $\alpha\text{-}\mathcal{T}_3$ lattice, which is formed by adding an additional atom to the unit cell of the graphene lattice with tunable coupling to the nearest atoms in the original honeycomb lattice¹⁰. The two limiting cases $\alpha = 0, 1$ correspond to graphene and dice lattice, respectively. The tight-binding Hamiltonian is

$$H_{\alpha\text{-}\mathcal{T}_3} = -t \begin{pmatrix} 0 & \cos \phi \Delta_{\mathbf{k}} & 0 \\ \cos \phi \Delta_{\mathbf{k}}^* & 0 & \sin \phi \Delta_{\mathbf{k}} \\ 0 & \sin \phi \Delta_{\mathbf{k}}^* & 0 \end{pmatrix}, \quad (7)$$

where $\Delta_{\mathbf{k}} = 2 \exp(-ik_x a/2) \cos(\sqrt{3}/2 k_y a) + \exp(ik_x a)$ and $\alpha \equiv \tan(\phi)$ for $0 \leq \phi \leq \pi/4$. The effective Hamiltonian is

$$H = \begin{pmatrix} 0 & f_{\mathbf{k}} \cos(\phi) & 0 \\ f_{\mathbf{k}}^* \cos(\phi) & 0 & f_{\mathbf{k}} \sin(\phi) \\ 0 & f_{\mathbf{k}}^* \sin(\phi) & 0 \end{pmatrix}, \quad (8)$$

where $f_{\mathbf{k}} = sk_x + ik_y$ and s is the valley index. For $s = 1$ there are three bands: $\tau = 0, \pm 1$, corresponding to a flat band, the conduction and valence bands, respectively. The eigenfunctions are

$$|\psi_{\tau=\pm 1}\rangle = \frac{1}{\sqrt{2}} \begin{pmatrix} (\cos \phi) e^{i\theta_{\mathbf{k}}} \\ \tau \\ (\sin \phi) e^{-i\theta_{\mathbf{k}}} \end{pmatrix}, \quad |\psi_{\tau=0}\rangle = \begin{pmatrix} (\sin \phi) e^{i\theta_{\mathbf{k}}} \\ 0 \\ -(\cos \phi) e^{-i\theta_{\mathbf{k}}} \end{pmatrix}, \quad (9)$$

where $\theta_{\mathbf{k}}$ is the phase angle of $f_{\mathbf{k}}$: $f_{\mathbf{k}} = |f_{\mathbf{k}}| e^{i\theta_{\mathbf{k}}}$. For the other valley, one has $f_{\mathbf{k},s=-1} = -f_{\mathbf{k},s=1}^*$, so the solution can be obtained from a simple sign change: $\theta_{\mathbf{k}} = -\theta_{\mathbf{k}}$.

For materials such as $\text{Hg}_{1-x}\text{Cd}_x\text{Te}$, theoretical computation⁸⁵ revealed their equivalence to the $\alpha\text{-}\mathcal{T}_3$ lattice with $\alpha = 1/\sqrt{3} \approx 0.58$. Experimental realizations of $\alpha\text{-}\mathcal{T}_3$ lattices have been achieved⁸⁶⁻⁸⁸.

E. Additional lattices with a flat band

Besides 2D lattices, a flat band can also arise in 1D lattices, which was experimentally demonstrated using a waveguide array to simulate the atomic interaction⁶⁹. Observation of localized flat-band modes was made in a quasi-1D photonic rhombic lattice⁸⁹. A flat band can also arise in 3D lattices^{90,91}, e.g., in lattices with a diamond structure⁹², where the transport behavior in the presence of impurities was studied⁹³. The Lieb lattice can be extended to three dimensions, leading to the Perovskite lattice⁹⁴ with band gap opening. A flat band can also occur in 3D Dirac semimetals⁹⁵. A tight-binding model for a 3D pyrochlore lattice was studied, revealing unusual flat band and also a flat-band enabled Weyl state⁹⁶. The theoretical predictions were verified by first-principle calculations based on $\text{Sn}_2\text{Nb}_2\text{O}_7$.

III. OPTICAL PROPERTIES OF 2D FLAT-BAND DIRAC-WEYL MATERIALS

The main motivation to investigate the optical properties of Dirac-Weyl materials with a flat band is that the flat band offers new possibilities for electronic transition, so the optical conductivity could be significantly enhanced as compared with graphene, making these flat-band materials better candidates for optical sensors and modulators. For example, it was demonstrated that, when an external electrical field is applied to a pseudospin-1 material, the induced current can be two times larger than that in graphene under nonequilibrium conditions⁹⁷, and the enhancement occurs in optical and magneto-optical conductivity^{58,98}. Due to the complications brought upon by the flat band, some existing studies focused only on the real part of the optical conductivity^{58,98-100}, leaving the crucial issue of optical absorption largely unaddressed. A recent work⁵⁶ filled this gap by deriving the full optical conductivity with both real and imaginary parts for the $\alpha\text{-}\mathcal{T}_3$ lattice using the Kubo formula^{50,58}. Alternatively, the formulas were derived⁵⁶ using the Kramers-Kronig method¹⁰¹.

There are three possible types of electronic transitions. For incident wave of relatively low frequency $\hbar\omega < \mu$, the intraband process dominates. For high frequency: $\hbar\omega > \mu$, two processes become important: the transition from the flat band to the Dirac cone and the cone-to-cone transition, where the former can be enhanced by increasing the value of α , e.g., the transition rate for pseudospin-1 materials can be twice as large as that in graphene⁹⁷. For the cone-to-cone transition, its rate is reduced with increasing α and becomes zero for $\alpha = 1$. The complete formulas of the optical conductivity are general because it does not depend on other material properties such as the Fermi velocity⁵⁶.

The starting point was to derive the optical matrix elements for the $\alpha\text{-}\mathcal{T}_3$ lattice. From the effective Hamiltonian (8), the current along the x direction is $j_x =$

$-ev_F S_x$, where

$$S_x = \begin{pmatrix} 0 & \cos \phi & 0 \\ \cos \phi & 0 & \sin \phi \\ 0 & \sin \phi & 0 \end{pmatrix}.$$

The matrix representation for the current operator is the optical matrix. The form of the eigenfunctions in Eq. (9)

indicate that, for $\mathbf{k} \neq \mathbf{k}'$, the expectation value of the current is zero¹⁰². For $\mathbf{k} = \mathbf{k}'$, one gets⁵⁸

$$\begin{aligned} |\langle \mathbf{k}, \tau = \pm | j_x | \mathbf{k}, \tau = \pm \rangle|^2 &= e^2 v_F^2 \cos^2 \theta_{\mathbf{k}}, \\ |\langle \mathbf{k}, \tau = \pm | j_x | \mathbf{k}, \tau = \mp \rangle|^2 &= e^2 v_F^2 \sin^2 \theta_{\mathbf{k}} \cos^2(2\phi), \\ |\langle \mathbf{k}, \tau = 0 | j_x | \mathbf{k}, \tau = \pm \rangle|^2 &= |\langle \mathbf{k}, \tau = \pm | j_x | \mathbf{k}, \tau = 0 \rangle|^2 \\ &= \frac{e^2 v_F^2}{2} \sin^2 \theta_{\mathbf{k}} \sin^2(2\phi). \end{aligned} \quad (10)$$

The general Kubo conductivity is

$$\sigma_{ij}(\omega, \phi) = \frac{\hbar}{2i\pi^2} \sum_{n,m} \frac{f(E_m) - f(E_n)}{E_n - E_m} \left(\frac{\langle n | j_i | m \rangle \langle m | j_j | n \rangle}{E_n - E_m - \hbar\omega} + \frac{\langle m | j_j | n \rangle \langle n | j_i | m \rangle}{E_m - E_n - \hbar\omega} \right), \quad (11)$$

where the subscripts i and j specify the directions of the current and of the electric field, respectively. For a homogeneous material and in the absence of any magnetic field, one has $\sigma_{xx} = \sigma_{yy}$ and $\sigma_{xy} = \sigma_{yx} = 0$. For simplicity, consider the case of $i = j = x$. The summation is for all the state with $|n\rangle = |\mathbf{k}, \tau\rangle$ and $|m\rangle = |\mathbf{k}', \tau'\rangle$. The quantity $f(E)$ in Eq. (11) is the Fermi-Dirac distribution function with a positive chemical potential μ .

Due to momentum conservation, the transitions from $|n\rangle$ and $|m\rangle$ are those among the energy bands. Let $\sigma^{(1)}(\omega, \phi)$, $\sigma^{(2)}(\omega, \phi)$ and $\sigma^{(3)}(\omega, \phi)$ denote the conductivity due to intraband, cone-to-cone and flat-to-cone transitions, respectively. For the intraband process, the transition is from the conduction band to itself with $E_n - E_m \rightarrow 0$ and $E_n \approx E_m \approx \mu$, leading to

$$\frac{f(E_m) - f(E_n)}{E_n - E_m} = - \left. \frac{\partial f}{\partial \epsilon} \right|_{\epsilon=\mu} = \delta(\epsilon - \mu),$$

so Eq. (11) becomes

$$\sigma^{(1)}(\omega, \phi) = \frac{\hbar}{i\pi^2} \iint dk_x dk_y \frac{\partial f}{\partial \epsilon} \frac{j_{nm}^2}{\hbar\omega}. \quad (12)$$

Inserting the optical matrix element in Eq. (10) into Eq. (12) and making use of the linear dispersion relationship $E = \hbar v_F |\mathbf{k}|$, in the polar coordinates, one gets

$$\iint dk_x dk_y j_{nm}^2 = \frac{e^2}{\hbar^2} \int_0^\infty \epsilon d\epsilon \int_0^{2\pi} \cos^2 \theta_{\mathbf{k}} d\theta. \quad (13)$$

Equation (12) becomes

$$\sigma^{(1)}(\omega, \phi) = \frac{e^2}{i\pi\hbar^2\omega} \int \epsilon [-\delta(\epsilon - \mu)] d\epsilon = \frac{ie^2\mu}{\pi\hbar^2\omega}. \quad (14)$$

With the notation $\sigma_0 \equiv e^2/(4\hbar)$, the intraband conductivity is

$$\sigma^{(1)}(\omega, \phi) = \frac{4i\mu\sigma_0}{\pi\hbar\omega}, \quad (15)$$

which is identical to the formula in other 2D materials such as graphene. The denominator indicates that the intraband conductivity dominates for small frequencies.

The cone-to-cone transitions can then be treated: those from $|\tau = -\rangle$ to $|\tau = +\rangle$ or vice visa (so there is an additional factor of two in the summation), leading to

$$\sigma^{(2)}(\omega, \phi) = \frac{\hbar}{i\pi^2} \sum_{n,m} \frac{f(E_m) - f(E_n)}{E_n - E_m} \frac{j_{nm}^2(-2\hbar\omega)}{(\hbar\omega) - (E_n - E_m)^2}.$$

For $\mathbf{k} = \mathbf{k}'$ and E_n and E_m belonging to different bands, one can write $E_n = \epsilon$ and $E_m = -\epsilon$. Using the integral from Eq. (13) and the optical matrix elements Eq. (10), one has

$$\sigma^{(2)}(\omega, \phi) = \cos^2(2\phi) \frac{e^2}{i\pi\hbar} \int [f(-\epsilon) - f(\epsilon)] \frac{\hbar\omega}{4\epsilon^2 - (\hbar\omega)^2} d\epsilon.$$

The Fermi-Dirac distribution implies nontrivial values of $\sigma^{(2)}(\omega, \phi)$ arise only for $\epsilon > \mu$ or $\epsilon < -\mu$ where, in the polar coordinates, only the first case contributes. This leads to

$$\sigma^{(2)}(\omega, \phi) = \cos^2(2\phi) \frac{e^2}{i\pi\hbar} \int_\mu^\infty \frac{\hbar\omega}{4\epsilon^2 - (\hbar\omega)^2} d\epsilon.$$

The integral has a singularity for $2\hbar\omega > \mu$. Using the residue theorem, one gets

$$\sigma^{(2)}(\omega, \phi) = \cos^2(2\phi) \sigma_0 \left[\Theta(\hbar\omega - 2\mu) - \frac{i}{\pi} \ln \left| \frac{\hbar\omega + 2\mu}{\hbar\omega - 2\mu} \right| \right], \quad (16)$$

where Θ is the Heaviside step function. It can be verified that, for $\phi = 0$, the result coincides with that for graphene. At the opposite end of the $\alpha\text{-}\mathcal{T}_3$ spectrum $\phi = \pi/4$ (pseudospin-1), the integral is zero.

The same method can be used to obtain the contribution of the flat-to-cone transitions to the optical conduc-

tivity. In this case, $E_n = 0$ and $E_m = \epsilon$, so

$$\sigma^{(3)}(\omega, \phi) = \sin^2(2\phi) \frac{e^2}{i\pi\hbar} \int_{\mu}^{\infty} \frac{\hbar\omega}{\epsilon^2 - (\hbar\omega)^2} d\epsilon,$$

where the singularity occurs at $\hbar\omega = \epsilon$ and the weight becomes $\sin^2(2\phi)$. Evaluating this integral gives

$$\sigma^{(3)}(\omega, \phi) = 2 \sin^2(2\phi) \sigma_0 \left[\Theta(\hbar\omega - \mu) - \frac{i}{\pi} \ln \left| \frac{\hbar\omega + \mu}{\hbar\omega - \mu} \right| \right]. \quad (17)$$

These conductivity formulas suggest that Dirac-Weyl flat-band materials can have significantly larger optical conductivity than that for graphene, due to the much stronger interaction between light and the lattice structure of the materials⁵⁶. As an example, Figs. 3(a), 3(c) and 3(e) show the real part of the finite-temperature optical conductivity for three different values of α , respectively, to which the intraband process has no contribution. For $\alpha = 0$ [graphene, Fig. 3(a)], only the cone-to-cone transition exists. For $\alpha = 1/\sqrt{3}$ [Fig. 3(c)], there are two transition points: cone-to-cone transition for $\hbar\omega/\mu > 2$ and flat-band-to-cone transition for $\hbar\omega/\mu > 1$. For $\alpha = 1$ [Fig. 3(e)], flat-band-to-cone transition is the only possibility and its magnitude is twice of that of the cone-to-cone transition for graphene. The respective imaginary parts of the conductivity are shown in Figs. 3(b), 3(d), and 3(f). In all three cases, the intraband process gives a singularity at $\omega \rightarrow 0$, and each interband transition leads to a dip for $\text{Im}(\sigma) < 0$. Note that the imaginary part of the conductivity can be negative. Previously, it was found for graphene that a negative imaginary part can lead to a special TE mode for electromagnetic wave propagation⁴⁴. For the $\alpha\mathcal{T}_3$ lattice, a negative imaginary part of the conductivity can have a significant effect on the intrinsic plasmon modes with respect to the loss, confinement and impurity scattering⁵⁶.

The formulas Eqs. (15), (16), and (17) give a complete description of the optical conductivity of the $\alpha\mathcal{T}_3$ lattice, which were verified⁵⁶ by an independent theoretical approach: the Kramers-Kronig formula. As examples of the application of the conductivity formulas, two phenomena were studied⁵⁶. First, while intraband transition leads to TM polarized waves at low frequencies (1–10 THz), TE polarized waves can emerge at high frequencies (100–300 THz), due to the two interband transitions. Second, the unique flat-band-to-cone transition generates multifrequency TE propagating waves and a strong optical response. These phenomena were numerically confirmed by the behaviors of propagating surface wave and scattering⁵⁶.

IV. DISCUSSION

In general, the optical responses of flat-band Dirac-Weyl materials are stronger than those of graphene, as

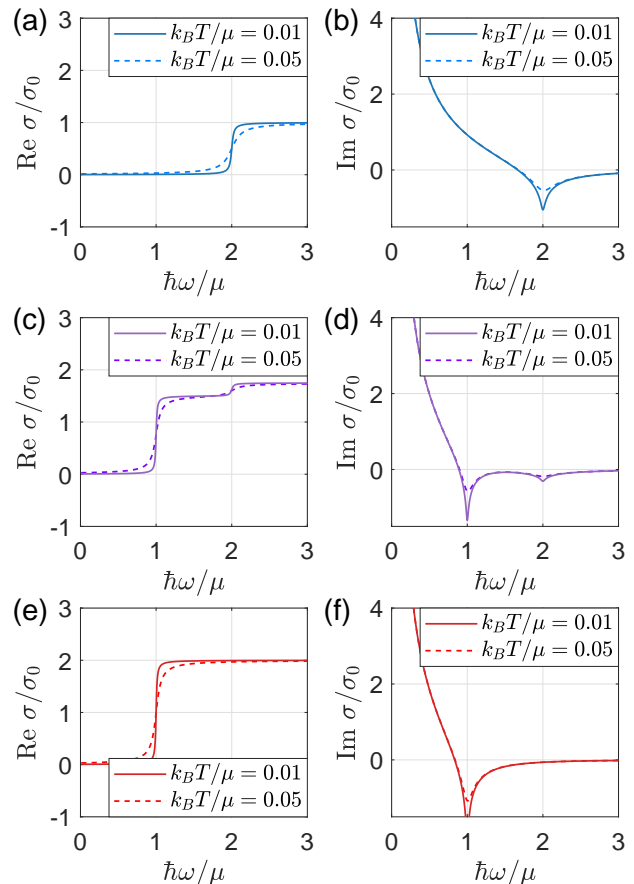


FIG. 3. Real and imaginary parts of the optical conductivity of the $\alpha\mathcal{T}_3$ lattice derived from the Kubo formula in the absence of any impurity scattering. (a,c,e) Real part of the optical conductivity for $\alpha = 0$ (graphene), $\alpha = 1/\sqrt{3}$, and $\alpha = 1$ (pseudospin-1), respectively. At zero temperature, the conductivity is nonzero for $\hbar\omega/\mu > 2$. An interband transition leads to a dip in the conductivity plot. The step-function type of transition is smoothed out by finite temperatures. (b,d,f) Imaginary part of the optical conductivity for $\alpha = 0, 1/\sqrt{3}$, and 1, respectively. Reprinted with permission from [C.-D. Han and Y.-C. Lai, “Optical response of two-dimensional Dirac materials with a flat band,” *Phys. Rev. B* 105, 155405 (2022)]. Copyright (2022) by the American Physical Society.

conductivity due to the flat-band-to-cone transition is twice of that induced by cone-to-cone transition. The physical reason behind is that the plane waves in these materials have a smaller attenuation length due to the large imaginary part of the optical conductivity as compared to that in graphene. This means that, at the same frequency, a larger scattering cross section can arise in flat-band Dirac-Weyl materials.

A complete description of the optical conductivity of flat-band Dirac-Weyl materials opens the door to investigating problems pertinent to development of optical devices. For example, intrinsic plasmon modes whose physical properties depend on the polarization were studied⁵⁶

with the finding that TM waves are the result of intra-band transitions, which usually occur in the frequency range 1–10 THz, but TE waves are the result of inter-band transitions, which can arise in a higher frequency range: 100–300 THz. When two interband transitions occurs (e.g., for $0 < \alpha < 1$ in the α - T_3 lattice), two TE surface waves can arise, respectively, at $\hbar\omega/\mu \approx 1, 2$. It was also suggested that TE polarized waves can be tuned by adjusting the chemical potential⁵⁶. Another example is scattering from a dielectric sphere coated with multiple layers of flat-band Dirac-Weyl material⁵⁶, where TM wave scattering can be stronger than TE wave, due to the reduced imaginary part of the optical conductivity at finite temperatures. This phenomenon can be exploited for enhancing certain desired polarization. A full optical conductivity theory allows electromagnetic dynamics in flat-band Dirac-Weyl materials to be studied in detail. Issues such as the emergence of intrinsic plasmon modes at a single or multiple frequencies, loss, attenuation length, and finite temperatures can be studied in detail. In fact, the occurrence of multi-frequency plasmon modes implies the possibility of achieving superscattering or cloaking at multiple frequencies. These broadband effects can find applications in optical sensing, imaging, tagging or spectroscopy^{103–105}. Moreover, edge states in graphene can lead to a blue shift in the plasmon modes¹⁰⁶. To exploit flat-band Dirac-Weyl materials for applications in quantum plasmonics could be an interesting area of research.

We briefly discuss the effects of impurities and many-body interaction on the optical response.

Effects of impurities. A number of previous works addressed this issue, but mainly for graphene. The general methodology is to start from the linear dispersion relationship and model the effects of defects or impurities on optical scattering through the incorporation of a relaxation time, taking into account electron-phonon scattering. For graphene, the relaxation time is relatively small, so it affects the low-frequency response more than the high-frequency response, rendering negligible the effect on optical response¹⁰⁷. In another work that went beyond the Dirac-cone approximation¹⁰⁸, the authors used the tight-binding model and the Kubo formula to study the effects of different types of impurities in graphene on the optical response, which included random potentials, random vacancies and random coupling, and found that the interband transition strength decreases with the impurity density. For example, for lattice vacancies, the interband transition is strong for 5% of the vacancies but is barely observable for 10% of the vacancies. For general types of impurities, their effects on the transition cannot be neglected. Since the impurities can generate states at $E = 0$, in graphene with defects, a transition at $\hbar\omega = \mu$ can occur. In a more recent work¹⁰⁹, hydrogen atoms as impurities were added to a graphene sheet at the density of approximately 300 impurity atoms per μm^2 . For $\mu = 2\text{eV}$, these impurities have negligible effect on the optical conduc-

tivity. However, for $\mu = 0.2\text{eV}$, an observable dip in the conductivity occurs at $\hbar\omega = 2\mu$.

For 2D pseudospin-1 Dirac materials with a flat band, the effects of impurities on optical response can be treated similarly by incorporating a finite relaxation time into the α - T_3 lattice⁵⁶. Under the same impurity conditions, for $\alpha = 1$ the interband transition is two times stronger than that in graphene, so this transition is more robust against defects or vacancies. It was found that, even when the relaxation time is several times smaller than that in graphene (corresponding to a more significant amount of impurities), the effects on the optical response in the high frequency regime are insignificant. In a recent work on the α - T_3 lattice¹¹⁰, the effects of lattice vacancies (up to 0.4%) leading to different inelastic-scattering rates on the density of states were studied and found to be negligible. However, the inelastic scattering can lead to a broadening of the flat band. In another recent work¹¹¹, the optical conductivity in α - T_3 lattice with a distorted flat band was studied and results similar to those in Ref. [56] were found, including the dependence of the conductivity on the temperature.

Effects of many-body interactions on optical response. In graphene, the electron self energy was used to describe the electron-electron interaction¹¹², and the scattering conductivity results were compared with the experimental measurements, validating the approach¹¹³. The electron-electron interactions and impurity scattering can reduce the transition strength by 20%. An increase in the real part of the conductivity at $\hbar\omega = 2\mu$ was observed for a wide interval of μ . It was also observed that the many-body effect and impurities in graphene create a non-zero optical conductivity for energy less than $\hbar\omega = 2\mu$, with the transition strength about 80% of that of the clean lattice. For 2D Dirac materials with a flat band, the combined lattice impurities and many-body interactions in general will lead to a reduction in the optical transition strength as compared with graphene, but the issue remains to be outstanding.

ACKNOWLEDGEMENT

This work was supported by AFOSR under Grant No. FA9550-21-1-0186.

- ¹B. Sutherland, “Localization of electronic wave functions due to local topology,” *Phys. Rev. B* **34**, 5208–5211 (1986).
- ²D. Bercioux, D. F. Urban, H. Grabert, and W. Häusler, “Massless Dirac-Weyl fermions in a T_3 optical lattice,” *Phys. Rev. A* **80**, 063603 (2009).
- ³R. Shen, L. B. Shao, B. Wang, and D. Y. Xing, “Single Dirac cone with a flat band touching on line-centered-square optical lattices,” *Phys. Rev. B* **81**, 041410 (2010).
- ⁴D. Green, L. Santos, and C. Chamon, “Isolated flat bands and spin-1 conical bands in two-dimensional lattices,” *Phys. Rev. B* **82**, 075104 (2010).
- ⁵B. Dóra, J. Kailasvuori, and R. Moessner, “Lattice generalization of the Dirac equation to general spin and the role of the flat band,” *Phys. Rev. B* **84**, 195422 (2011).

- ⁶F. Wang and Y. Ran, “Nearly flat band with Chern number $c=2$ on the dice lattice,” *Phys. Rev. B* **84**, 241103 (2011).
- ⁷X. Huang, Y. Lai, Z. H. Hang, H. Zheng, and C. T. Chan, “Dirac cones induced by accidental degeneracy in photonic crystals and zero-refractive-index materials,” *Nat. Mater.* **10**, 582 (2011).
- ⁸J. Mei, Y. Wu, C. T. Chan, and Z.-Q. Zhang, “First-principles study of Dirac and Dirac-like cones in phononic and photonic crystals,” *Phys. Rev. B* **86**, 035141 (2012).
- ⁹P. Moitra, Y. Yang, Z. Anderson, I. I. Kravchenko, D. P. Briggs, and J. Valentine, “Realization of an all-dielectric zero-index optical metamaterial,” *Nat. Photon.* **7**, 791–795 (2013).
- ¹⁰A. Raoux, M. Morigi, J.-N. Fuchs, F. Piéchon, and G. Montambaux, “From dia- to paramagnetic orbital susceptibility of massless fermions,” *Phys. Rev. Lett.* **112**, 026402 (2014).
- ¹¹D. Guzmán-Silva, C. Mejía-Cortés, M. A. Bandres, M. C. Rechtsman, S. Weimann, S. Nolte, M. Segev, A. Szameit, and R. A. Vicencio, “Experimental observation of bulk and edge transport in photonic Lieb lattices,” *New J. Phys.* **16**, 063061 (2014).
- ¹²J. Romhányi, K. Penc, and R. Ganesh, “Hall effect of triplons in a dimerized quantum magnet,” *Nat. Commun.* **6**, 6805 (2015).
- ¹³G. Giovannetti, M. Capone, J. van den Brink, and C. Ortix, “Kekulé textures, pseudospin-one Dirac cones, and quadratic band crossings in a graphene-hexagonal indium chalcogenide bilayer,” *Phys. Rev. B* **91**, 121417 (2015).
- ¹⁴Y. Li, S. Kita, P. Muoz, O. Reshef, D. I. Vulis, M. Yin, M. Lonar, and E. Mazur, “On-chip zero-index metamaterials,” *Nat. Photon.* **9**, 738–742 (2015).
- ¹⁵S. Mukherjee, A. Spracklen, D. Choudhury, N. Goldman, P. Öhberg, E. Andersson, and R. R. Thomson, “Observation of a localized flat-band state in a photonic Lieb lattice,” *Phys. Rev. Lett.* **114**, 245504 (2015).
- ¹⁶R. A. Vicencio, C. Cantillano, L. Morales-Inostroza, B. Real, C. Mejía-Cortés, S. Weimann, A. Szameit, and M. I. Molina, “Observation of localized states in Lieb photonic lattices,” *Phys. Rev. Lett.* **114**, 245503 (2015).
- ¹⁷S. Taie, H. Ozawa, T. Ichinose, T. Nishio, S. Nakajima, and Y. Takahashi, “Coherent driving and freezing of bosonic matter wave in an optical Lieb lattice,” *Sci. Adv.* **1**, e1500854 (2015).
- ¹⁸A. Fang, Z. Q. Zhang, S. G. Louie, and C. T. Chan, “Klein tunneling and supercollimation of pseudospin-1 electromagnetic waves,” *Phys. Rev. B* **93**, 035422 (2016).
- ¹⁹F. Diebel, D. Leykam, S. Kroesen, C. Denz, and A. S. Desyatnikov, “Conical diffraction and composite Lieb bosons in photonic lattices,” *Phys. Rev. Lett.* **116**, 183902 (2016).
- ²⁰L. Zhu, S.-S. Wang, S. Guan, Y. Liu, T. Zhang, G. Chen, and S. A. Yang, “Blue phosphorene oxide: Strain-tunable quantum phase transitions and novel 2D emergent fermions,” *Nano Lett.* **16**, 6548–6554 (2016).
- ²¹B. Bradlyn, J. Cano, Z. Wang, M. G. Vergniory, C. Felser, R. J. Cava, and B. A. Bernevig, “Beyond Dirac and Weyl fermions: Unconventional quasiparticles in conventional crystals,” *Science* **353** (2016).
- ²²I. C. Fulga and A. Stern, “Triple point fermions in a minimal symmorphic model,” *Phys. Rev. B* **95**, 241116 (2017).
- ²³M. Ezawa, “Triplet fermions and Dirac fermions in borophene,” *Phys. Rev. B* **96**, 035425 (2017).
- ²⁴C. Zhong, Y. Chen, Z.-M. Yu, Y. Xie, H. Wang, S. A. Yang, and S. Zhang, “Three-dimensional pentagon carbon with a genesis of emergent fermions,” *Nat. Commun.* **8**, 15641 (2017).
- ²⁵Y.-Q. Zhu, D.-W. Zhang, H. Yan, D.-Y. Xing, and S.-L. Zhu, “Emergent pseudospin-1 Maxwell fermions with a threefold degeneracy in optical lattices,” *Phys. Rev. A* **96**, 033634 (2017).
- ²⁶R. Drost, T. Ojanen, A. Harju, and P. Liljeroth, “Topological states in engineered atomic lattices,” *Nat. Phys.* **13**, 668 (2017).
- ²⁷M. R. Slot, T. S. Gardenier, P. H. Jacobse, G. C. van Miert, S. N. Kempkes, S. J. Zevenhuizen, C. M. Smith, D. Vanmaekelbergh, and I. Swart, “Experimental realization and characterization of an electronic Lieb lattice,” *Nat. Phys.* **13**, 672–676 (2017).
- ²⁸X. Tan, D.-W. Zhang, Q. Liu, G. Xue, H.-F. Yu, Y.-Q. Zhu, H. Yan, S.-L. Zhu, and Y. Yu, “Topological Maxwell metal bands in a superconducting qutrit,” *Phys. Rev. Lett.* **120**, 130503 (2018).
- ²⁹W. Jiang, X. Ni, and F. Liu, “Exotic topological bands and quantum states in metal-organic and covalent-organic frameworks,” *Acc. Chem. Res.* **54**, 416–426 (2021).
- ³⁰X.-J. Ni, H. Li, F. Liu, and J.-L. Bredas, “Engineering of flat bands and Dirac bands in two-dimensional covalent organic frameworks (COFs): relationships among molecular orbital symmetry, lattice symmetry, and electronic-structure characteristics,” *Mater. Horiz.* **9**, 88–98 (2022).
- ³¹A. Vakil and N. Engheta, “Transformation optics using graphene,” *Science* **332**, 1291–1294 (2011).
- ³²A. Grigorenko, M. Polini, and K. Novoselov, “Graphene plasmonics,” *Nat. Photonics* **6**, 749–758 (2012).
- ³³Q. Bao and K. P. Loh, “Graphene photonics, plasmonics, and broadband optoelectronic devices,” *ACS Nano* **6**, 3677–3694 (2012).
- ³⁴Q. Bao, H. Zhang, B. Wang, Z. Ni, C. H. Y. X. Lim, Y. Wang, D. Y. Tang, and K. P. Loh, “Broadband graphene polarizer,” *Nat. Photonics* **5**, 411–415 (2011).
- ³⁵L. Ju, B. Geng, J. Horng, C. Girit, M. Martin, Z. Hao, H. A. Bechtel, X. Liang, A. Zettl, Y. R. Shen, *et al.*, “Graphene plasmonics for tunable terahertz metamaterials,” *Nat. Nanotechnol.* **6**, 630–634 (2011).
- ³⁶I. F. Akyildiz, J. M. Jornet, and C. Han, “Terahertz band: Next frontier for wireless communications,” *Phys. Commun.* **12**, 16–32 (2014).
- ³⁷W. Li, B. Chen, C. Meng, W. Fang, Y. Xiao, X. Li, Z. Hu, Y. Xu, L. Tong, H. Wang, *et al.*, “Ultrafast all-optical graphene modulator,” *Nano Lett.* **14**, 955–959 (2014).
- ³⁸M. Baudisch, A. Marini, J. D. Cox, T. Zhu, F. Silva, S. Teichmann, M. Massicotte, F. Koppens, L. S. Levitov, F. J. G. de Abajo, *et al.*, “Ultrafast nonlinear optical response of Dirac fermions in graphene,” *Nat. Commun.* **9**, 1–6 (2018).
- ³⁹P.-Y. Chen and A. Alu, “Atomically thin surface cloak using graphene monolayers,” *ACS Nano* **5**, 5855–5863 (2011).
- ⁴⁰R. Li, X. Lin, S. Lin, X. Liu, and H. Chen, “Tunable deep-subwavelength superscattering using graphene monolayers,” *Opt. Lett.* **40**, 1651–1654 (2015).
- ⁴¹C.-D. Han and Y.-C. Lai, “Generating extreme quantum scattering in graphene with machine learning,” *Phys. Rev. B* **106**, 214307 (2022).
- ⁴²S. Thongrattanasiri, F. H. Koppens, and F. J. G. De Abajo, “Complete optical absorption in periodically patterned graphene,” *Phys. Rev. Lett.* **108**, 047401 (2012).
- ⁴³H. Meng, Q. Lin, X. Xue, J. Lian, G. Liu, W. Xu, X. Zhai, Z. Liu, J. Chen, H. Li, *et al.*, “Ultrathin multi-band coherent perfect absorber in graphene with high-contrast gratings,” *Opt. Expr.* **28**, 24285–24297 (2020).
- ⁴⁴S. A. Mikhailov and K. Ziegler, “New electromagnetic mode in graphene,” *Phys. Rev. Lett.* **99**, 016803 (2007).
- ⁴⁵G. W. Hanson, “Dyadic Green’s functions and guided surface waves for a surface conductivity model of graphene,” *J. Appl. Phys.* **103**, 064302 (2008).
- ⁴⁶A. Y. Nikitin, F. Guinea, F. García-Vidal, and L. Martín-Moreno, “Edge and waveguide terahertz surface plasmon modes in graphene microribbons,” *Phys. Rev. B* **84**, 161407 (2011).
- ⁴⁷G. Ni, H. Wang, J. Wu, Z. Fei, M. Goldflam, F. Keilmann, B. Özyilmaz, A. C. Neto, X. Xie, M. Fogler, *et al.*, “Plasmons in graphene Moiré superlattices,” *Nat. Mater.* **14**, 1217–1222 (2015).
- ⁴⁸X. Lin, Z. Liu, T. Stauber, G. Gómez-Santos, F. Gao, H. Chen, B. Zhang, and T. Low, “Chiral plasmons with twisted atomic bilayers,” *Phys. Rev. Lett.* **125**, 077401 (2020).
- ⁴⁹B. Deng, C. Ma, Q. Wang, S. Yuan, K. Watanabe, T. Taniguchi, F. Zhang, and F. Xia, “Strong mid-infrared photoresponse in small-twist-angle bilayer graphene,” *Nat. Photonics* **1**, 1–5

- (2020).
- ⁵⁰L. Falkovsky and A. Varlamov, "Space-time dispersion of graphene conductivity," *Eur. Phys. J. B* **56**, 281–284 (2007).
 - ⁵¹Y. Gao, G. Ren, B. Zhu, H. Liu, Y. Lian, and S. Jian, "Analytical model for plasmon modes in graphene-coated nanowire," *Opt. Expr.* **22**, 24322–24331 (2014).
 - ⁵²T. Stauber, N. Peres, and A. Geim, "Optical conductivity of graphene in the visible region of the spectrum," *Phys. Rev. B* **78**, 085432 (2008).
 - ⁵³T. Christensen, A.-P. Jauho, M. Wubs, and N. A. Mortensen, "Localized plasmons in graphene-coated nanospheres," *Phys. Rev. B* **91**, 125414 (2015).
 - ⁵⁴J. Wang, X. Sui, S. Gao, W. Duan, F. Liu, and B. Huang, "Anomalous Dirac plasmons in 1D topological electrides," *Phys. Rev. Lett.* **123**, 206402 (2019).
 - ⁵⁵J. Wang, X. Sui, W. Duan, F. Liu, and B. Huang, "Density-independent plasmons for terahertz-stable topological metamaterials," *Proc. Nat. Acad. Sci. (USA)* **118**, e2023029118 (2019).
 - ⁵⁶C.-D. Han and Y.-C. Lai, "Optical response of two-dimensional Dirac materials with a flat band," *Phys. Rev. B* **105**, 155405 (2022).
 - ⁵⁷H.-Y. Xu and Y.-C. Lai, "Revival resonant scattering, perfect caustics, and isotropic transport of pseudospin-1 particles," *Phys. Rev. B* **94**, 165405 (2016).
 - ⁵⁸E. Illes, J. Carbotte, and E. Nicol, "Hall quantization and optical conductivity evolution with variable Berry phase in the α - T_3 model," *Phys. Rev. B* **92**, 245410 (2015).
 - ⁵⁹M. Rizzi, V. Cataudella, and R. Fazio, "Phase diagram of the bose-hubbard model with T_3 symmetry," *Phys. Rev. B* **73**, 144511 (2006).
 - ⁶⁰D. Leykam and S. Flach, "Perspective: Photonic flatbands," *APL Photon.* **3**, 070901 (2018).
 - ⁶¹S. Mukherjee, M. Di Liberto, P. Öhberg, R. R. Thomson, and N. Goldman, "Experimental observation of Aharonov-Bohm cages in photonic lattices," *Phys. Rev. Lett.* **121**, 075502 (2018).
 - ⁶²D. Leykam, A. Andreanov, and S. Flach, "Artificial flat band systems: from lattice models to experiments," *Adv. Phys. X* **3**, 1473052 (2018).
 - ⁶³N. A. Franchina Vergel, L. C. Post, D. Sciacca, M. Berthe, F. Vaurette, Y. Lambert, D. Yarekha, D. Troadec, C. Coinon, G. Fleury, *et al.*, "Engineering a robust flat band in III-V semiconductor heterostructures," *Nano Lett.* (2020).
 - ⁶⁴T. Horiguchi and C. Chen, "Lattice Green's function for the diced lattice," *J. Math. Phys.* **15**, 659–660 (1974).
 - ⁶⁵J. Vidal, R. Mosseri, and B. Douçot, "Aharonov-Bohm cages in two-dimensional structures," *Phys. Rev. Lett.* **81**, 5888–5891 (1998).
 - ⁶⁶J. Vidal, G. Montambaux, and B. Douçot, "Transmission through quantum networks," *Phys. Rev. B* **62**, R16294 (2000).
 - ⁶⁷D. Bercioux, M. Governale, V. Cataudella, and V. M. Ramaglia, "Rashba effect in quantum networks," *Phys. Rev. B* **72**, 075305 (2005).
 - ⁶⁸E. H. Lieb, "Two theorems on the Hubbard model," *Phys. Rev. Lett.* **62**, 1201–1204 (1989).
 - ⁶⁹H. Tasaki, "Hubbard model and the origin of ferromagnetism," *Eur. Phys. J. B* **64**, 365–372 (2008).
 - ⁷⁰V. Apaja, M. Hyrkäs, and M. Manninen, "Flat bands, Dirac cones, and atom dynamics in an optical lattice," *Phys. Rev. A* **82**, 041402 (2010).
 - ⁷¹M. Niță, B. Ostahie, and A. Aldea, "Spectral and transport properties of the two-dimensional Lieb lattice," *Phys. Rev. B* **87**, 125428 (2013).
 - ⁷²C.-Z. Wang, H.-Y. Xu, and Y.-C. Lai, "Super skew scattering in two-dimensional Dirac material systems with a flat band," *Phys. Rev. B* **103**, 195439 (2021).
 - ⁷³W. Jiang, H. Huang, and F. Liu, "A Lieb-like lattice in a covalent-organic framework and its stoner ferromagnetism," *Nat. Commun.* **10**, 2207 (2019).
 - ⁷⁴I. Syôzi, "Statistics of Kagomé lattice," *Prog. Theor. Phys.* **6**, 306–308 (1951).
 - ⁷⁵M. Mekata, "Kagome: The story of the basketweave lattice," *Phys. Today* **56**, 12 (2003).
 - ⁷⁶H.-M. Guo and M. Franz, "Topological insulator on the Kagome lattice," *Phys. Rev. B* **80**, 113102 (2009).
 - ⁷⁷E. Tang, J.-W. Mei, and X.-G. Wen, "High-temperature fractional quantum Hall states," *Phys. Rev. Lett.* **106**, 236802 (2011).
 - ⁷⁸R. Chisnell, J. Helton, D. Freedman, D. Singh, R. Bewley, D. Nocera, and Y. Lee, "Topological magnon bands in a Kagome lattice ferromagnet," *Phys. Rev. Lett.* **115**, 147201 (2015).
 - ⁷⁹Z. F. Wang, N. Su, and F. Liu, "Prediction of a two-dimensional organic topological insulator," *Nano Lett.* **13**, 2842–2845 (2013).
 - ⁸⁰M. Pan, X. Zhang, Y. Zhou, P. Wang, Q. Bian, H. Liu, X. Wang, X. Li, A. Chen, X. Lei, S. Li, Z. Cheng, Z. Shao, H. Ding, J. Gao, F. Li, and F. Liu, "Growth of mesoscale ordered two-dimensional hydrogen-bond organic framework with the observation of flat band," *Phys. Rev. Lett.* **130**, 036203 (2023).
 - ⁸¹Y. Zhou, G. Sethi, C. Zhang, X. Ni, and F. Liu, "Giant intrinsic circular dichroism of enantiomorphic flat Chern bands and flatband devices," *Phys. Rev. B* **102**, 125115 (2020).
 - ⁸²Y. Zhou, G. Sethi, H. Liu, Z. Wang, and F. Liu, "Excited quantum anomalous and spin Hall effect: dissociation of flatbands-enabled excitonic insulator state," *Nanotech.* **33**, 415001 (2022).
 - ⁸³G. Sethi, Y. Zhou, L. Zhu, L. Yang, and F. Liu, "Flat-band-enabled triplet excitonic insulator in a diatomic Kagome lattice," *Phys. Rev. Lett.* **126**, 196403 (2021).
 - ⁸⁴G. Sethi, M. Cuma, and F. Liu, "Excitonic condensate in flat valence and conduction bands of opposite chirality," *Phys. Rev. Lett.* **130**, 186401 (2023).
 - ⁸⁵J. D. Malcolm and E. J. Nicol, "Magneto-optics of massless Kane fermions: Role of the flat band and unusual Berry phase," *Phys. Rev. B* **92**, 035118 (2015).
 - ⁸⁶F. Teppe, M. Marcinkiewicz, S. S. Krishtopenko, S. Ruffenach, C. Consejo, A. Kadykov, W. Desrat, D. But, W. Knap, J. Ludwig, *et al.*, "Temperature-driven massless Kane fermions in HgCdTe crystals," *Nat. Commun.* **7**, 1–6 (2016).
 - ⁸⁷A. Charukha, A. Sternbach, H. Stinson, R. Schlereth, C. Brüne, L. W. Molenkamp, and D. Basov, "Ultrafast nonlocal collective dynamics of Kane plasmon-polaritons in a narrow-gap semiconductor," *Sci. Adv.* **5**, eaau9956 (2019).
 - ⁸⁸S. Hubmann, G. V. Budkin, M. Otteneder, D. But, D. Sacré, I. Yahniuk, K. Diendorfer, V. V. Bel'kov, D. A. Kozlov, N. N. Mikhailov, S. A. Dvoretzky, V. S. Varavin, V. G. Remesnik, S. A. Tarasenko, W. Knap, and S. D. Ganichev, "Symmetry breaking and circular photogalvanic effect in epitaxial $\text{Cd}_x\text{Hg}_{1-x}\text{Te}$ films," *Phys. Rev. Mater.* **4**, 043607 (2020).
 - ⁸⁹S. Mukherjee and R. R. Thomson, "Observation of localized flat-band modes in a quasi-one-dimensional photonic rhombic lattice," *Opt. Lett.* **40**, 5443–5446 (2015).
 - ⁹⁰M. Orlita, D. Basko, M. Zholudev, F. Teppe, W. Knap, V. Gavrilenko, N. Mikhailov, S. Dvoretzky, P. Neugebauer, C. Faugeras, *et al.*, "Observation of three-dimensional massless Kane fermions in a zinc-blende crystal," *Nat. Phys.* **10**, 233–238 (2014).
 - ⁹¹N. J. Ghimire and I. I. Mazin, "Topology and correlations on the Kagome lattice," *Nat. Mater.* **19**, 137–138 (2020).
 - ⁹²S. Nishino and M. Goda, "Three-dimensional flat-band models," *J. Phys. Soc. Jpn.* **74**, 393–400 (2005).
 - ⁹³M. Goda, S. Nishino, and H. Matsuda, "Inverse Anderson transition caused by flatbands," *Phys. Rev. Lett.* **96**, 126401 (2006).
 - ⁹⁴C. Weeks and M. Franz, "Topological insulators on the Lieb and perovskite lattices," *Phys. Rev. B* **82**, 085310 (2010).
 - ⁹⁵S. M. Young, S. Zaheer, J. C. Teo, C. L. Kane, E. J. Mele, and A. M. Rappe, "Dirac semimetal in three dimensions," *Phys. Rev. Lett.* **108**, 140405 (2012).

- ⁹⁶Y. Zhou, K.-H. Jin, H. Huang, Z. Wang, and F. Liu, “Weyl points created by a three-dimensional flat band,” *Phys. Rev. B* **99**, 201105 (2019).
- ⁹⁷C.-Z. Wang, H.-Y. Xu, L. Huang, and Y.-C. Lai, “Nonequilibrium transport in the pseudospin-1 Dirac-Weyl system,” *Phys. Rev. B* **96**, 115440 (2017).
- ⁹⁸Y.-R. Chen, Y. Xu, J. Wang, J.-F. Liu, and Z. Ma, “Enhanced magneto-optical response due to the flat band in nanoribbons made from the α - T_3 lattice,” *Phys. Rev. B* **99**, 045420 (2019).
- ⁹⁹C. Tabert, J. Carbotte, and E. Nicol, “Optical and transport properties in three-dimensional Dirac and Weyl semimetals,” *Phys. Rev. B* **93**, 085426 (2016).
- ¹⁰⁰Á. D. Kovács, G. Dávid, B. Dóra, and J. Cserti, “Frequency-dependent magneto-optical conductivity in the generalized α - T_3 model,” *Phys. Rev. B* **95**, 035414 (2017).
- ¹⁰¹T. Stauber, P. San-Jose, and L. Brey, “Optical conductivity, Drude weight and plasmons in twisted graphene bilayers,” *New J. Phys.* **15**, 113050 (2013).
- ¹⁰²L. L. Y. Voon and L. Ram-Mohan, “Tight-binding representation of the optical matrix elements: Theory and applications,” *Phys. Rev. B* **47**, 15500 (1993).
- ¹⁰³M. Danilov, R. DeVoe, A. Dolgolenko, G. Giannini, G. Gratta, P. Picchi, A. Piepke, F. Pietropaolo, P. Vogel, J. Vuilleumier, *et al.*, “Detection of very small neutrino masses in double-beta decay using laser tagging,” *Phys. Rev. B* **480**, 12–18 (2000).
- ¹⁰⁴P. Del’Haye, T. Herr, E. Gavartin, M. L. Gorodetsky, R. Holzwarth, and T. J. Kippenberg, “Octave spanning tunable frequency comb from a microresonator,” *Phys. Rev. Lett.* **107**, 063901 (2011).
- ¹⁰⁵A. Schliesser, N. Picqué, and T. W. Hänsch, “Mid-infrared frequency combs,” *Nat. Photonics* **6**, 440–449 (2012).
- ¹⁰⁶K. O. Wedel, N. A. Mortensen, K. S. Thygesen, and M. Wubs, “Emergent scale invariance of nonclassical plasmons in graphene nanoribbons,” *Phys. Rev. B* **98**, 155412 (2018).
- ¹⁰⁷M. Jablan, H. Buljan, and M. Soljačić, “Plasmonics in graphene at infrared frequencies,” *Phys. Rev. B* **80**, 245435 (2009).
- ¹⁰⁸S. Yuan, R. Roldán, H. De Raedt, and M. I. Katsnelson, “Optical conductivity of disordered graphene beyond the Dirac cone approximation,” *Phys. Rev. B* **84**, 195418 (2011).
- ¹⁰⁹G. Viola, T. Wenger, J. Kinaret, and M. Fogelström, “Graphene plasmons in the presence of adatoms,” *New J. Phys.* **19**, 073027 (2017).
- ¹¹⁰H.-L. Liu, J. Wang, and J.-F. Liu, “Chiral zero-energy modes in the disordered α - T_3 lattice,” *Phys. Rev. B* **107**, 125412 (2023).
- ¹¹¹A. Iurov, L. Zhemchuzhna, G. Gumbs, and D. Huang, “Optical conductivity of gapped α - T_3 materials with a deformed flat band,” *Phys. Rev. B* **107**, 195137 (2023).
- ¹¹²A. G. Grushin, B. Valenzuela, and M. A. H. Vozmediano, “Effect of Coulomb interactions on the optical properties of doped graphene,” *Phys. Rev. B* **80**, 155417 (2009).
- ¹¹³Z. Li, E. A. Henriksen, Z. Jiang, Z. Hao, M. C. Martin, P. Kim, H. L. Stormer, and D. N. Basov, “Dirac charge dynamics in graphene by infrared spectroscopy,” *Nat. Phys.* **4**, 532–535 (2008).